Control of a Closed Separation Domain in Adverse Pressure Gradient Over a Curved Surface

C. J. Peterson, B. Vukasinovic, and A. Glezer

Woodruff School of Mechanical Engineering, Georgia Institute of Technology, Atlanta, GA 30332-0405.

Abstract

A closed separation domain in an adverse pressure gradient on a curved surface in a high-speed small-scale tunnel is controlled at $M = 0.25$ using fluidic actuation by a spanwise array of oscillating jets. The actuation effects on the topology of the separation domain are investigated with specific emphasis on its local separation and reattachment points, including the global and local characteristic scales and turbulent structure. As the actuation level increases, the separation domain undergoes three distinct stages: initial enlargement, rapid diminution, and, finally, asymptotic extinction. Although the actuation nearly halves the base flow's turbulent kinetic energy at both separation and reattachment, the magnitude of the cross-stream vorticity flux decreases at separation, while it remains nearly invariant at reattachment. The present investigations show that despite the distinct differences between the cross-stream scales of the mean velocity profiles at separation and reattachment in the presence and absence of actuation, scaling of these profiles by parameters associated with the outer shear layer yields remarkable collapse of all profiles except very close to the surface. Furthermore, that this similarity holds for both closed and open controlled separation domains in an adverse pressure gradient implies that these separating flows may be governed by a similar inviscid mechanism.

I. Background

Internal flows with imposed adverse pressure gradients are highly susceptible to local, sustained flow separation that can lead to flow instabilities and significant losses. Active flow control can potentially mitigate these adverse effects by delaying separation or bypassing it altogether.

The severe losses that are associated with internal flow separation have motivated numerous investigations of the fundamental aspects of these complex flows over the years in various geometries such as flow junctions (e.g., Ethier, et al. [1]), convex banks (Blanckaert [2]), backward facing steps (Papadopoulos and Otugen [3]), and curved ducts (Yang et al. [4]), to name a few. Investigations of active control of internal flow separation have received considerable attention since the 1950s. Suzuki et al. [5] considered flow separation in a two-dimensional diffuser and its control by periodic mass injection. Their reduced-order model study showed alteration of vortex formation and dynamics in the controlled flows that led to a reduction of the separation bubble albeit with negligible changes in the separation location. Studies by Amitay et al. [6] demonstrated the effectiveness of active flow control in delaying internal separation in a duct having a rectangular cross section and reported a reduction in the streamwise scale of the separation domain and concomitant increase in the volume flow rate and reduction in losses in the presence of flow actuation. In a related investigation, Kumar and Alvi [7] demonstrated the feasibility of another

flow control element, a high-speed micro-jet, for suppressing flow separation at $M < 0.2$. Banaszuk et al. [8] demonstrated the application of an adaptive flow control scheme for multi-frequency flow separation control in a planar diffuser by utilization of synthetic jets. Vaccaro et al. [9] investigated mitigation of internal flow separation in a compact rectangular offset duct using steady blowing at the flow boundary (up to $M \approx 0.45$) and showed that changes in flow attachment can affect total pressure recovery and distortion in the affected flow segment.

Analysis and comparison of internal flow separation characteristics with and without flow control are also considered in the present work. Simpson [10] notes that turbulent separation has a much different structure than that for attached flows. Some of the defining characteristics are that the largest turbulent stresses occur within the middle of free shear layer due to occurrences of large scale vortices, which have a complex effect on pressure fluctuations and the recirculation zone. Due to the complex interactions, the separation is inherently unsteady. Of further interest is the modification of the natural turbulent separation structure under the flow control. An example of control of a shear flow is studied for the flows over a backwards facing step [11,12,13]. The study by Chun and Sung [11] demonstrates that a localized forcing effect near the separation point has significant effect on the characteristics of the separated flow structure. Specifically, the roll up procedure in the shear layer is changed, which results in varying the vortex entrainment and furthermore the reattachment length off of the step.

In addition to the time-invariant effects of flow control on the nominally time-averaged spatial delay (or displacement) of the separation, another important aspect of the actuation is its effect on the flow dynamics about the new location of separation which can have significant impact on global flow stability. In a review of aspects of turbulent flow separation, Simpson [10] noted that a defining characteristic of separated flow is the large turbulent stress within the separated shear layer that is associated with the formation of large-scale vortices that effect pressure fluctuations and coupled unsteady pressure-velocity oscillations in the recirculating flow domain. The effects of separation control on the unsteady flow features of flow separation reattachment are of particular interest. Chun and Sung [11], Yoshioka et al., [12] and Vukasinovic et al. [13] investigated control of separating flow at a fixed separation point, formed by an abrupt change in the flow boundary over a backward-facing step. Chun and Sung [11] demonstrated that acoustic forcing near the separation point had significant effect on the characteristics of the separated flow structure by altering the roll-up of the forming vortices and thereby varying entrainment and, ultimately, the reattachment length downstream of the step. Yoshioka et al. [12] showed that the effects of actuation on flow reattachment downstream of the backward-facing step increased production of the Reynolds stresses. Vukasinovic et al. [13] attributed the increased turbulent kinetic energy production and dissipation within the separated shear layer to high-frequency (dissipative) actuation at the location of separation.

As well as the dynamics about the separation, of interest are the characteristics of the separation bubble itself and its ensuing changes with flow control. Pauley, Moin, and Reynolds [14] studied the structure of two-dimensional laminar separation via time-accurate numerical simulations. They determined that a strongly imposed adverse pressure gradient caused the flow to separate and shed vortices with regular frequency. They also determined that ‘bursting’ observed in experiments, occurred under the same conditions as the periodic shedding in the simulations, suggesting that bursting, was actually periodic shedding having been smoothed out by time-averaging of the data. Kiya and Sasaki [15] studied the nature of a highly unsteady, turbulent separation bubble on the sides of a blunt flat plate. They found that, not only does the bubble shed

vortices with regular frequency (similar to the findings for a laminar bubble by Pauley, Moin, and Reynolds [14]), but that there is still a large-scale unsteadiness inherent in the bubble. This large-scale unsteadiness is accompanied by a dynamic enlargement and shrinking of the bubble, as well as a 'flapping' motion of the outer bounding shear layer. They expand on the nature of the separation bubble further, in their later work focused on the reverse flow near the reattaching zone of the bubble [16]. They found that the separation bubble experiences the shrinkage and enlargement in connection with the low-frequency unsteadiness of the bubble, but that the speed of shrinkage is much larger than that of the enlargement of the bubble. Furthermore, they develop a model that suggests the large-scale vortices in the reattaching zone are hairpin vortices with each of the ends rotating in opposite directions, such that the fluid is actually lifted between them. Dandois, Garnier and Sagaut [17] simulated the effects of synthetic jet forcing on a generic separated flow over a smooth ramp. They found that two modes of the forcing by the synthetic jet are observed for which the separation length is reduced: a vorticity-dominated mode at low operation frequencies, and an acoustic-dominated mode at higher frequency forcing cases. They observed that in the low frequency, vorticity-dominated mode, the forcing is correlated to an increase of the turbulent kinetic energy as well as increased entrainment into the separation bubble.

The changes of the dynamics in the flow due to actuation, consequently, have drastic changes in the shape of the turbulent boundary layer approaching separation and reattachment. As such, the shape of the turbulent boundary changes where the energy bearing fluctuations and stresses are located. Marusic and Perry [18] defined two distinct types of eddies to describe the energy-containing motion within a turbulent boundary layer. Type-A eddies are considered wall structures and produce finite Reynolds stress at the wall, while Type-B eddies are wake structures and give a zero Reynolds shear stress at the wall. They postulate that these two variations of eddies can account for all possible boundary layer states including both equilibrium and non-equilibrium boundary layers. Ellsberry et al. [19], noted that boundary layers maintained close to separation over extended distances give rise to nearly linear streamwise growth of integral length scales, and that the boundary layer maintained in a non-equilibrium state required different scales to collapse the velocity and turbulence intensity profiles. Castillo and George [20] commented further saying that most turbulent boundary layers appear to be equilibrium similarity boundary layers when the pressure gradient parameter Λ = constant, contrary to classical belief that equilibrium flows are difficult to achieve. Furthermore, there are three values associated with the pressure gradient parameter defining adverse, favorable, and zero pressure gradient equilibrium conditions. More recently, Schatzman and Thomas [21] concluded that for turbulent boundary layers exposed to adverse pressure gradients of sufficient magnitude to give rise to an inflectional mean profile, the flow is largely governed by the existence of an outer embedded shear layer. They also stated that separation is not required for the existence of the embedded shear layer, which gives rise to the ability to create a scaling parameter based off of outer flow features. Peterson, Vukasinovic, and Glezer [22] investigated the dynamics and characteristic structure of natural and deliberately-delayed, migrated separating flow within a severe adverse pressure gradient and concluded that, despite expected differences in the flow dynamics about local flow separation, there is an underlying similar flow structure. Moreover, it was found that arguments made about flow being governed by an embedded shear layer [21] can be extended to not only naturally-separating flow, but also to the controlled flow separation, such is in the diffusing duct.

The present experimental study focuses on assessing the characteristic properties of flow separation in an adverse pressure gradient, which results in a closed separation domain. In particular, emphasis is placed on the changes in the flow separation features as natural separation

becomes delayed by application of active flow control, which affects not only the local flow separation but also its reattachment.

II. Experimental Setup and Methodology

The experiments are performed in a small, open-return, subsonic blow down wind tunnel, where the temperature of the return air is controlled using a low pressure drop heat exchanger. The tunnel terminates in a nominally free jet discharge station that is coupled to a test geometry. The test geometry (Figure 1) consists of a nominal inlet duct of $W \times H = 2H$ cross-section, where the channel height $H = 127$ mm, and test section length is $L = 660.4$ mm. The shown test section is coupled to the outlet of the tunnel facility using an adapter section (not shown) that is filled with honeycomb and a mesh screen to provide uniform inflow to the test section. A slim-profile Pitot probe is integrated into the test section at the inlet plane for characterization of the oncoming flow Mach number, which is nominally set to $M = 0.25$. This probe is paired with the wall static pressure in the same plane, and this measured static pressure, along with the calculated Mach number at the test section inlet, are used as reference values for the flow characterization. Both the total and static pressure ports at the test section inlet are measured by two *baratron* pressure transducers and sampled by a DAQ computer. The central symmetry plane of the model also contains a number of static surface pressure ports that are measured by a dedicated *PSI* Netscanner system. Each set of those measurements is based on sixty-four independent samples, while the mean static and total pressures are based on seventy-five data sets. Furthermore, four temperature transducers are distributed from the inlet into the facility to just upstream from the test section, and are monitored and recorded during data acquisition. Finally, a PIV setup is utilized for flow characterization through the test section. For that purpose, the PIV laser sheet passes through the bottom optical window (Figure 1) illuminating the central vertical plane. The side walls of the test section are made of acrylic, and the PIV camera is positioned normal to the laser sheet, mounted on a computer-controlled x-y traversing mechanism. PIV measurements are typically done in multiple, partially-overlapping fields of view along the central plane, in order to preserve fine spatial resolution over the wide measurement domain. All the individual flow fields are integrated into a composite flow field during post-processing. Each set of PIV measurements is taken at 200 Hz and ensemble averages are based on over 1,000 image pairs.

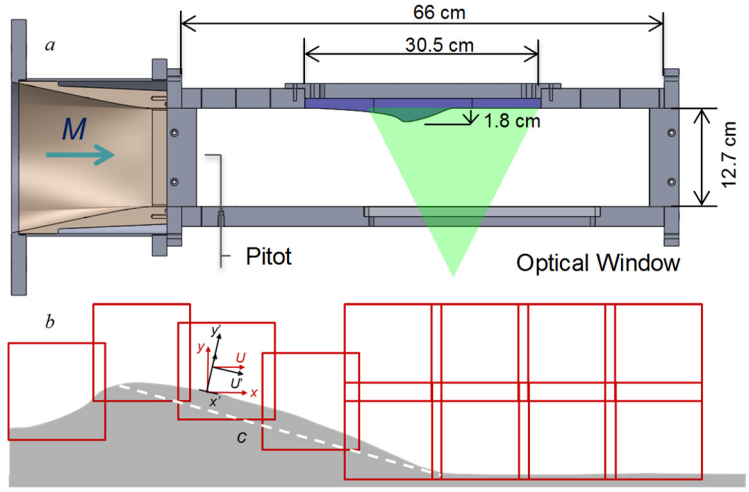

Figure 1. *Flow geometry (a) and zoomed-in view of twelve partially-overlapping individual PIV windows (b). Fixed (x.y) and wall-normal (x',y') coordinate systems are shown for reference.*

Test model geometry is based on a VR-12 airfoil at a 13 degrees angle of attack, with a chord length of $c \approx 62.7$ mm (Figure 1), which is chosen such to impose significant adverse pressure gradient to induce flow separation. To further promote flow separation, a trip wire (dia. ~0.43 mm) is mounted upstream from the airfoil model surface at $x =$ 320mm ($x/c = 5.1$) downstream of the test section inlet. The baseline geometry is built out of the three integrated segments, such that the central one can be interchanged with a module populated with the flow

control jets. Flow control is effected by fluidic oscillating jets, which have already been utilized in a number of internal and external flow control applications. These jets combine the benefits of unsteady flow control due to their oscillating nature and a net addition of mass and momentum to the flow. Another important aspect of this flow control approach is in utilization of the Coanda effect along the surface of the test geometry as the jest are issued along a convex surface. In addition, their simplicity of operation and low maintenance requirements make them suitable candidates for airborne applications. An array of 17 equally-spaced jets are deployed in the current study at a constant streamwise location $x/c = 5.4$ across the span of the test geometry. The jets, which orifices measure 0.5 × 1 mm on the sides, are spaced 7 mm apart. The jets nominal issuing direction is tangential to the surface moldline, while they oscillate in the spanwise direction. The jet oscillating frequency is a weak function of the fluidic oscillator flow rate and, for typical flow rates utilized in the current test, the frequency is on the order of 10 kHz. The flow control parameter is defined as the mass flow rate coefficient $C_\mu = Thrust_{jet}/\rho_\infty A_\infty V^2_\infty$, which is the ratio between the total momentum through the jet array and the momentum through the test section.

III. The Base Flow

Initial characterization of the base flow is shown as static streamwise surface pressure measurements along the central plane. Figure 2 shows the variation in the corresponding pressure coefficient $C_p = (2/\gamma M^2_\infty)(p/p_\infty - 1)$ along the center line of the test section for varying inlet Mach number, M. As M increases (shown as darkening colors in Figure 2), there is an increase in the suction peak over the model apex due to higher flow accelerations, before the pressure begins to recover due to the transition from favorable to adverse pressure gradients over the model surface. As the boundary layer becomes continuously diffuse under the adverse pressure gradient, it eventually separates at the first region of interest for the current study – the origin of the flow separation, which is marked by the red dashed line at $x/c \approx 5.25$. Once the flow separates, the outer pressure remains governed by the changing, confined flow geometry, and some pressure recovery is measured even over the separated flow extent, as indicated by a slight increase in the C_p levels within the separated domain. At the termination of the convex ramp geometry, the pressure gradient transitions from adverse to favorable. However, since the flow is separated, the pressure gradient within the domain changes and does not demonstrate the same pressure gradient as the outer flow. The separated flow eventually reattaches at $x/c \approx 6.25$, which represents the second relevant domain of interest (marked by the blue dashed line in Figure 2). It is noted that there is little appreciable migration of the separation domain (i.e. separation bubble) ($5.25 < x/c < 6.25$) with increasing M for base flow conditions. Although there is no significant migration of the separation bubble, there is a slight change in the pressure gradient within the separated domain, as shown by the

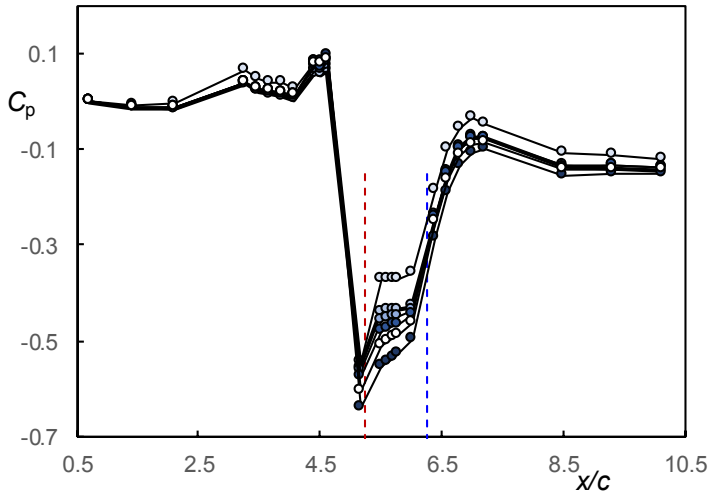

Figure 2. *Distributions of the base flow pressure coefficient along the centerline for the oncoming M = 0.08 – 0.31 (top to bottom). Nominal M = 0.25 is shown in white symbols.*

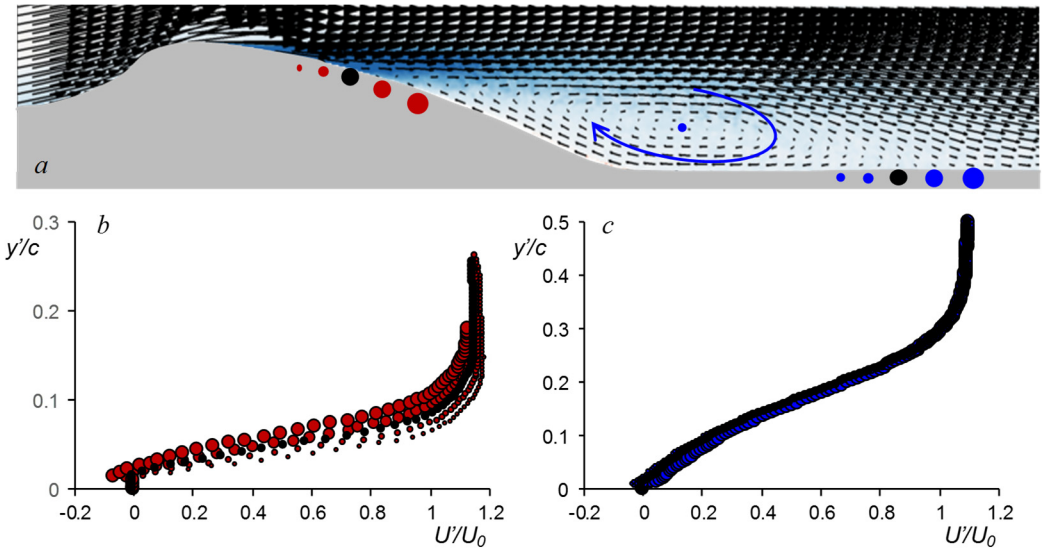

Figure 3. *Raster plots of the mean vorticity with overlaid mean velocity vectors for the base flow at M = 0.25 (a) and the mean velocity profiles through the flow* ***separation*** *(b) and* ***reattachment*** *(c). Symbol size increases in the downstream direction, and central profile is anchored at separation/reattachment point. At separation x/c =* (·) *5.27,* (•) *5.29,* (•) *5.32,* (•) *5.34, and* (•) *5.37, and for reattachment x/c =* (·) *6.43,* (•) *6.45,* (•) *6.48,* (•) *6.50, and* (•) *6.53.*

varying slope in the C_p between the dashed marks. This continually-changing gradient points to the differences in the cross-stream scale of the bubble with changing M, despite little change in its streamwise extent. Lastly, regardless of the notable changes in C_p profiles downstream from the surface apex, there is just a small offset among all of the measured profiles upstream from the apex ($x/c < 5.0$), which is attributed to a nearly self-similar upstream flow evolution that is independent of the oncoming Mach number. In the remainder of the presented work, the oncoming Mach number is set nominally to $M = 0.25$ (open symbols in Figure 2).

As already stated, the primary interest of the present study is in characterization of the flow separation and reattachment regions. For that purpose, particle image velocimetry is the primary tool for investigating the flow fields about these locations, as well as within the separation bubble. As outlined in Figure 1b, multiple high-resolution PIV fields of view are measured and combined to create composite views of the flow domains that maintain this high spatial resolution throughout. To illustrate such a composite base flow field at $M = 0.25$, Figure 3a shows an ensemble-averaged raster plot of the spanwise vorticity component, along with overlaid equidistant mean velocity vectors. The mean recirculating bubble is fully captured in this composite view, and it is marked on the flow field. Furthermore, the local flow separation and reattachment points are marked by black dots, the difference of which indicates the streamwise extent of the separation domain, L_x. To illustrate how the flow progresses through separation and reattachment, two upstream and two downstream velocity profiles relative to the separation/reattachment points are chosen, equally spaced ~1.6 mm ($\Delta x/c$ =0.025). The resulting mean wall-normal (U') velocity profiles are shown in Figures 3b and c, for the flow evolving through separation and reattachment, respectively. The symbol sizes indicate the evolutionary direction of the profiles, as shown schematically in Figure 3a. As the base, unactuated flow evolves through separation, the velocity profiles shown in Figure 3b progressively stretch away from the wall, even over a short streamwise distance, due to the strong adverse pressure gradient. Consequently, the embedded shear extends and becomes gradually displaced away from the surface as well. Opposite to the growing shear/vorticity layer present in the velocity profiles about the separation point, equidistant velocity profiles at the local

reattachment region (Figure 3c), show nearly invariant evolution over the same total distance. This is primarily attributed to the pressure gradient transitioning from adverse to weakly favorable in the test section, which consequently has less intense effect on the flow evolution. This mild evolution of the mean velocity profiles at reattachment relative to the separation point also indicates less transfer of momentum and consequently, mixing, that is associated with this reattached flow, compared to the separating one.

IV. Controlled Flow Separation

An analysis of the static centerline surface pressure profiles for an oncoming flow $M = 0.25$, is done to initially characterize the actuation effect on the base flow separation. Analogous to the base flow characterization (Figure 2), streamwise distributions of the pressure coefficients are shown in Figure 4 while varying the control flow parameter C_μ. The symbol shape represents an increasing level of C_μ that spans $0 < C_\mu \cdot 10^3 < 2.1$, while the base flow is shown in open symbols for reference. An excellent collapse of the pressure coefficient profiles both upstream and downstream of the separated domain, is noted, which emphasizes the highly localized effect of the flow control upon the separation bubble ($5.25 < x/c < 6.25$ for the base flow). Interestingly, for the lowest level of C_μ ($C_\mu\ 10^3 = 0.36$), there is actually a small deceleration of the flow at the apex, followed by a shallower pressure gradient throughout the separation bubble, which suggests a somewhat adverse effect of the actuation at the lowest C_μ. Such a pressure distribution further suggests that the separation domain likely becomes somewhat enlarged, even though it may not be captured in the streamwise resolution of the static pressure port locations. However, as C_μ increases, the flow control's effect on the pressure distribution switches. The suction (negative) peak at the apex increases, indicating further accelerated flow as the outer flow is further entrained over the surface, which is then able to withstand higher levels of the adverse pressure gradient downstream from the apex, which shifts the separation point downstream, highlighted by elevated C_p levels within the separation domain with increasing actuation C_μ. It is clearly seen that the segment of the C_p profiles containing the separation bubble shortens in both the upstream and downstream extent with further increase in C_μ, indicating the separation bubble shrinks from both ends (i.e. upstream and downstream directions). This bubble suppression evolves up to $C_\mu\ 10^3 = 2.1$ when there is uninterrupted pressure recovery across the whole aft section of the surface profile, indicating that the flow remains fully attached throughout this region, and the separation bubble is fully suppressed. Once the flow is reattached, further increasing C_μ serves only to increase the suction peak at the apex through enhanced flow acceleration, which in turn assists in slightly higher pressure recovery at the downstream end of the surface model.

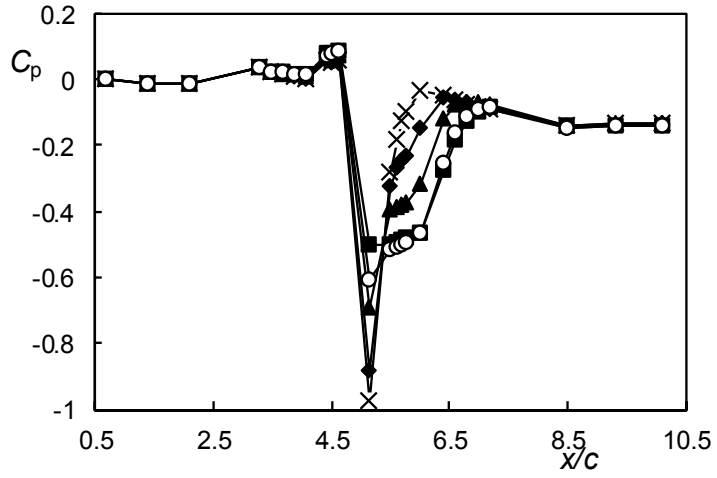

Figure 4. *Distributions of the pressure coefficient along the centerline for the base (○, M = 0.25) and the flow controlled by $C_\mu \cdot 10^3$ = 0.36 (■), 0.96 (▲), 1.5 (♦), and 2.1 (×).*

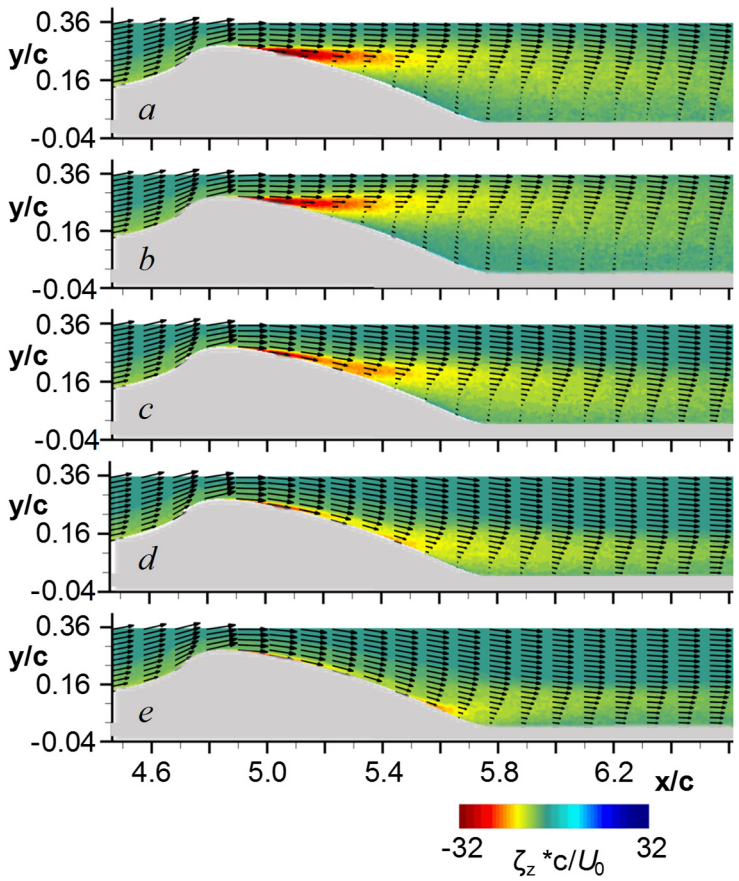

Figure 5. *Raster plots of the mean vorticity with overlaid mean velocity profiles at M = 0.25 and for the jet momentum coefficient $C_\mu \cdot 10^3$ = 0 (a), 0.36 (b), 0.96 (c), 1.5 (d), 2.1 (e).*

The full flow field PIV measurements, as outlined in Figure 1b, are done for several characteristic flow control cases, based on the pressure coefficient profiles shown in Figure 4. Five composite flow fields are shown in Figure 5 as raster plots of the mean spanwise vorticity overlaid with equidistant mean velocity vectors for four levels of actuation C_μ. Figure 5a shows the base flow field for reference. The base flow was already discussed in connection to Figure 3a and is marked by incipient flow separation off the aft side of the surface profile at $x/c \approx 5.2$. Consequently, the separated shear layer rapidly evolves along the oncoming flow direction, marked by diffusion of the initially concentrated vorticity layer. As the separated flow traverses towards the end of the geometrically-imposed adverse pressure gradient, it begins to deflect back toward the surface and reattaches at $x/c \approx 6.4$. As suggested by the surface pressure evolution for $C_\mu \cdot 10^3 = 2.1$ (Figure 4), this low level of actuation does not delay the flow separation (Figure 5b). Instead, this level of actuation appears to slightly deflect the separating shear layer away from the surface (compare its initial direction to that of Figure 5a). The outward vectoring of the initial shear layer away from the surface causes the separated region characteristic cross-stream scale to increase, which inevitably leads to an increase in the downstream location (i.e. delayed) reattachment as well. This is clearly seen at the downstream end of the measurement domain, as the flow now reattaches at $x/c \approx 6.5$. In agreement with the pressure profiles in Figure 4, however, all higher levels of C_μ progressively delay the flow separation and reduce the recirculating domain. Already at $C_\mu \cdot 10^3 = .96$ (Figure 5c), a notable reduction in the separated domain is captured, where both the separation and reattachment points are displaced closer to each other. Additionally, the separating shear layer is clearly conforming much better, and entrained, to the surface, being vectored downward. As the vorticity layer becomes increasingly wall bound with further increase in C_μ (Figures 5d and e), this additionally impedes mixing in this flow and limits the growth of the shear layer. It is interesting to note that even when the flow remains fully attached throughout the aft flow domain, there is still a remnant of wall-bound vorticity, as seen in Figure 5e.

As both the flow separation and reattachment points move with the application of flow control, further analysis of the flow control's effect on the separation domain is done by extracting wall-normal velocity profiles centered at separation and reattachment, with progressing C_μ. For each

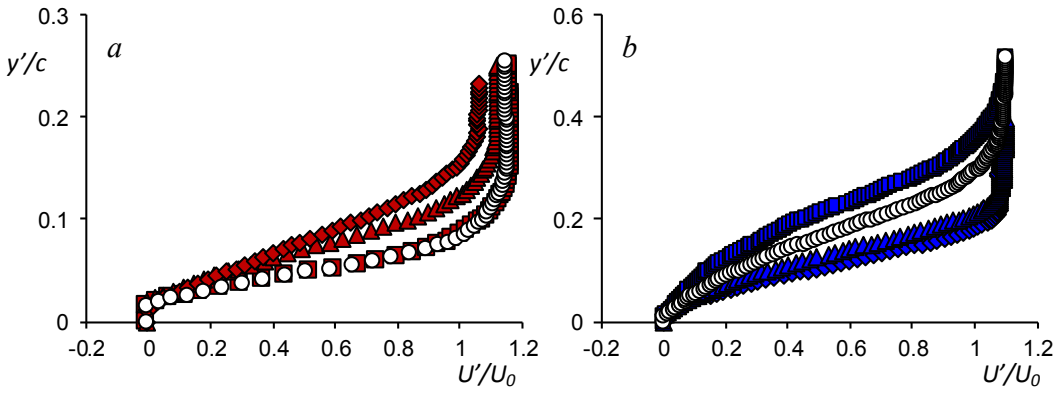

Figure 6. *Mean velocity profiles at separation (a) and reattachment (b) for the base (○, M = 0.25) and the flow controlled by $C_\mu \cdot 10^3$ = 0.36 (□), 0.96 (Δ), and 1.5 (◊). At **separation** x/c = (○) 5.32, (■) 5.27, (▲) 5.53, (♦) 5.71 and at **reattachment** = (○) 6.48, (■) 6.59, (▲) 6.20, (♦) 5.95.*

of the flow fields shown in Figure 5, wall-normal velocity profiles (U') centered at separation and reattachment are shown in Figures 6a and b, respectively. A two-fold stretching in the cross-stream direction of the velocity profiles between the separation and reattachment is measured. When examining the separation velocity profiles (Figure 6a), it is seen that despite the vectoring of the vorticity layer away from the wall with small levels of actuation (cf. Figure 5b, $C_\mu \cdot 10^3$ = 0.36), there is little appreciable change in the mean velocity profile at separation relative to the base flow. As C_μ increases, there is a stretching of the cross-stream scale of the velocity profile, having a central extent that is nearly-linear. The profiles' inflection point (contained within this embedded shear layer) becomes displaced away from the wall, indicating a concurrent displacement of the origin of the ensuing shear layer. At the same time, a decreasing velocity gradient points to the reduction in the magnitude of the shear with C_μ. It is noted that the constant velocity away from the surface decreases with C_μ, as the delayed flow separation allows the bulk flow to diffuse farther, along the surface geometry. When examining the mean profile evolution at reattachment (Figure 6b), the first noticeable difference is that the wall-normal terminal velocity does not change appreciably between the base flow and actuated cases, unlike the profiles about separation, which is attributed to the full-expanded bulk flow being contained in the constant-area cross section, downstream from the model. Another difference is that increasing the level of actuation moves the inflection point closer to the wall, while limiting the cross-stream scale of the velocity profile. Also, the velocity profile for the lowest level of actuation ($C_\mu \cdot 10^3$ = 0.36) clearly indicates an increase in the cross-stream extent of the shear layer, and further develops a possible secondary inflection point in the mean velocity profile.

The differences seen in the mean velocity profiles and their respective inflection points bear consequences on characteristics of the flow stability, that was already reflected in the migration and reduction of peak magnitude of the vorticity layer distribution over the surface, as discussed in Figure 5. These differences clearly point to altered flow field dynamics in the presence of actuation, which is further assessed in terms of the turbulent kinetic energy $\left(\overline{u'^2} + \overline{v'^2}\right)/2$ and shear stress distributions ($\overline{u'v'}$) presented in Figure 7. Contour plots of these quantities are shown for all of the flow conditions presented in Figure 5. As expected, the elevated levels of both of the

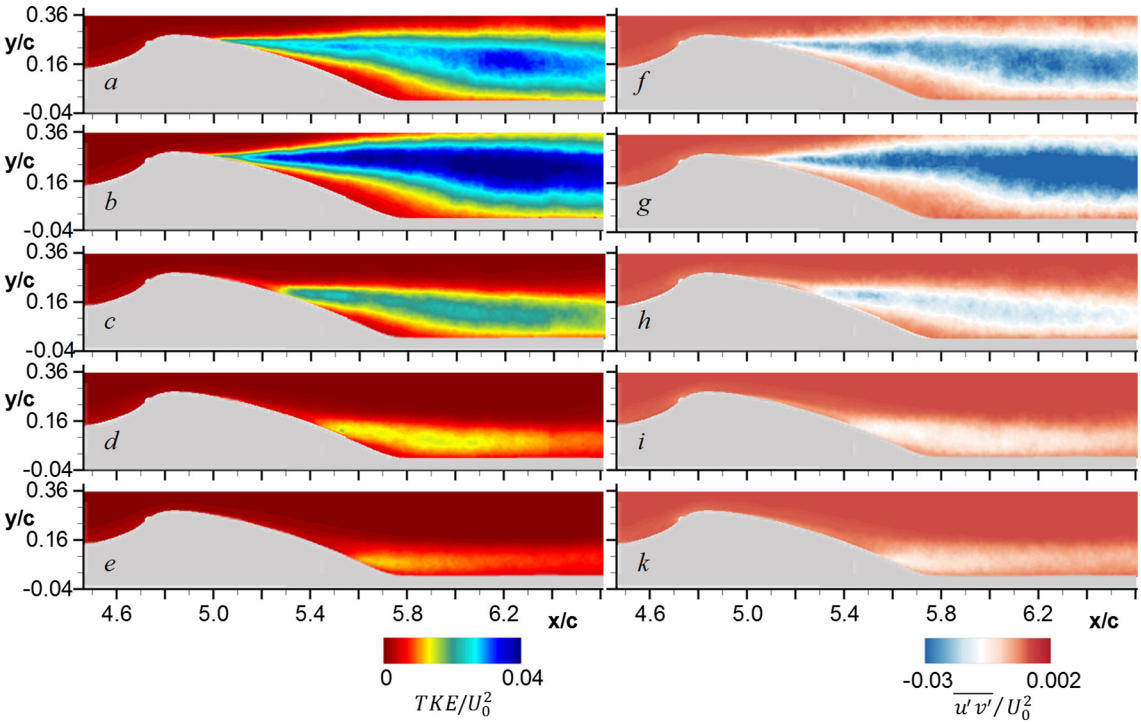

Figure 7. *Raster plots of turbulent kinetic energy (a–e) and turbulent shear stress (f–k) for the jet momentum coefficient $C_\mu \cdot 10^3$ = 0 (a,f), 0.36 (b,g), 0.96 (c,h), 1.5 (d,i), 2.1 (e,k).*

turbulent parameters in Figure 7 are closely associated with the location of the shear layers present in each of the respective fields (Figure 5). It is noteworthy that the peak TKE levels of the base flow (Figure 7a) are clearly extracted at about x/c = 6.2 in the shear layer, which is attributed to the formation of large-scale coherent structures. No other controlled case indicates such a focused node of the peak TKE, which is indicative of a disruptive effect to large-scale coherent motions due to the flow control [13]. Furthermore, it is seen in all of the controlled flow realizations in Figure 7, that the TKE and the shear stress distributions respond similarly to actuation; not only are they displaced and confined over smaller domains, following the altered shear layers, but the overall magnitude levels become reduced with further delays in separation (i.e. increasing C_μ). The only condition that stands out from this trend is again the case for the lowest actuation level ($C_\mu \cdot 10^3 = 0.36$) (Figures 7b and g), where not only the streamwise and cross-stream extent of the elevated turbulent levels are increased relative to its base flow counterparts, but there is a clear increase in their peak magnitude levels as well. Both observations are attributed to increased large-scale, energy-bearing, unsteady motions brought about by the vectoring of the shear layer and increase of the separated domain. Lastly, it should be noted that, just like in the discussion of vorticity levels in the attached flow (cf. Figure 5e), there are still regions of somewhat elevated turbulent stresses, even when the flow control is shown to maintain attached flow over the whole surface (in the average sense). This further suggests that such a fully-attached flow in the averaged sense is likely still unsteady and separated at times, but prevailingly attached in the dynamic sense.

Prior to a more detailed analysis of the flow characteristics undergoing separation and reattachment, the suppression of the separation bubble in the presence of flow control is examined. Based on the flow fields depicted in Figures 5 and 7, for the base flow, and each of the three controlled flow fields exhibiting a clear separation bubble, are used for extraction of the corresponding separation and reattachment points x^*, where x^* = 0 is at the base flow separation

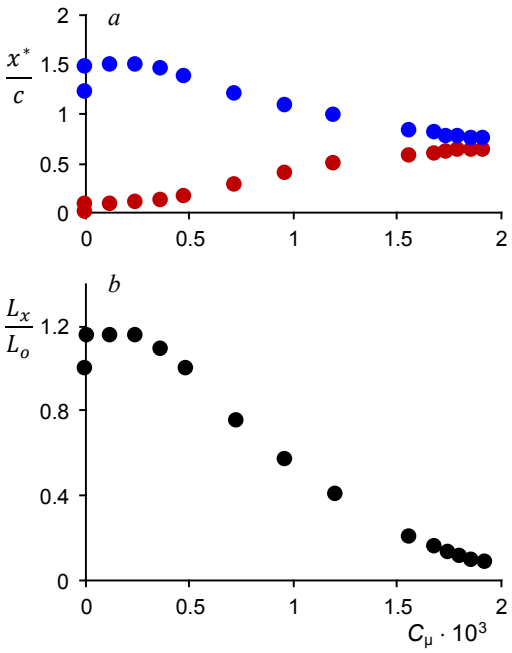

Figure 8. *Migration of the separation (●) and reattachment (●) point, and the separation axial extent (●) with jet momentum coefficient C_μ*

point. The axial distance between two such points defines the characteristic streamwise length of the bubble L_x. In order to gain higher resolution of the bubble response to the flow control parameter C_μ, additional partial PIV flow fields are measured for a range of C_μ, where each of the PIV windows was located about the separation/reattachment point for each C_μ. Therefore, although no full flow field information is obtained, these targeted PIV measurements provide sufficient information to determine the separation bubble's streamwise scale. Therefore, a number of pairs of points corresponding to the flow separation and reattachment migration with C_μ is extracted, and these two progressions are shown in Figure 8a. It is interesting that for the smallest level of actuation, the separation point immediately moves downstream, which is then followed by a somewhat lessened response for the next three consecutive C_μ levels. Similarly, the reattachment point responds sharply for the lowest C_μ, and it also moves downstream. The next three responses are significantly smaller, but still indicate the growth of the separation bubble on the downstream end. Finally, the bubble begins to shrink on both sides at $C_\mu \cdot 10^3 = 0.24$, when the reattachment point begins to move upstream. Soon thereafter, is the sharpest response to actuation, where both ends of the bubble appear to be shrinking at similar rates. As the bubble begins to shrink further and become closer to the fully attached condition, the final response of the separation domain reaches an almost asymptotic rate of response at the tail end of C_μ, where it only incrementally shrinks on both ends with increases in C_μ. The full bubble rate of change, relative to the base flow bubble scale L_o is shown in Figure 8b. Clearly, immediately after the flow control is applied at the lowest levels of C_μ, the separation bubble sharply grows by about 15% in the streamwise direction, which is completely facilitated by the downstream displacement of the reattachment point. As it peaks in length at that level, it begins to retreat, reverting to its initial length Lo at about $C_\mu \cdot 10^3 = 0.48$. After that, the bubble appears to be the most responsive to actuation, shrinking rapidly to $0.2 \cdot L_o$ by $C_\mu \cdot 10^3 = 1.56$. Finally, as already mentioned in the discussion of Figure 8a, the last stage of the bubble suppression occurs at a much lower rate, and for the last 12%, it takes $C_\mu \cdot 10^3 = 2.16$ until the flow remains fully attached throughout and the bubble is bypassed.

Of particular interest in the present investigation is the examination of how the flow changes as it passes through separation and reattachment, and even more so, what are the similarities and differences between these two processes when the flow is controlled in such a way that it remains attached further into the adverse pressure gradient, or when it reattaches upstream from its natural reattachment zone. Figure 9 illustrates some of the key features of the flow passing through delayed separation when the nominal $M = 0.25$ flow is controlled by $C_\mu \cdot 10^3 = 1.5$. Profiles of the wall-normal velocity U', vorticity flux, and turbulent kinetic energy are shown in black at

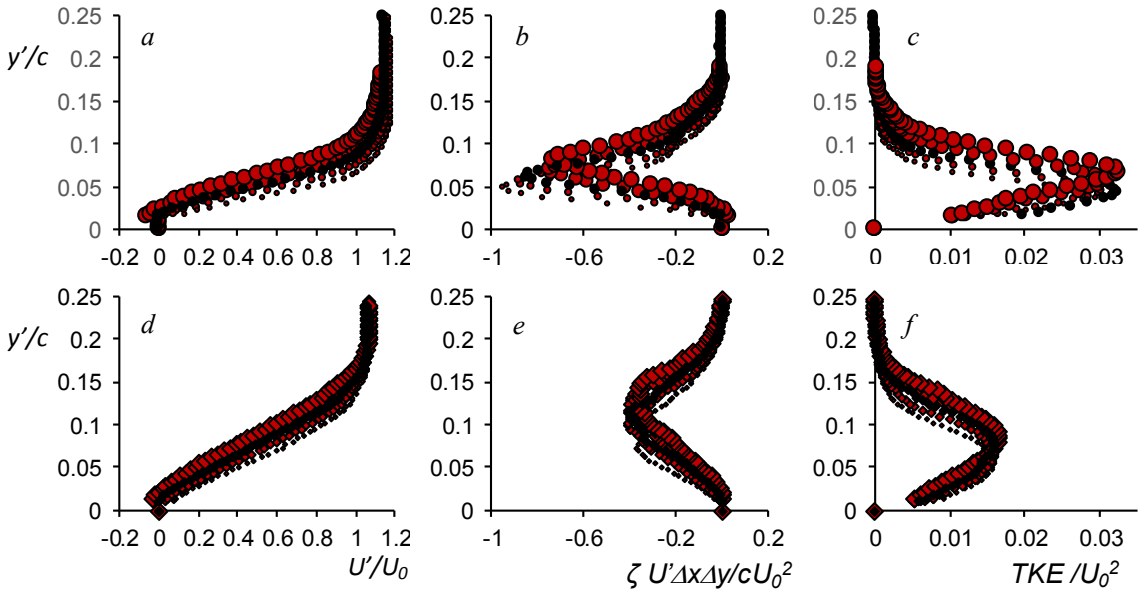

Figure 9. *Evolution of the mean velocity (a,d), vorticity flux (b,e) and turbulent kinetic energy (c,f) profiles through the flow separation for $C_\mu \cdot 10^3 = 0$ (a–c) and 1.5 (d–f). Symbol size increases in the downstream direction, and black symbols are associated with the separation point. At separation for $C_\mu \cdot 10^3 = 0$, x/c = (·) 5.27, (•) 5.29, (•) 5.32, (•) 5.34, and (•) 5.37, and for $C_\mu \cdot 10^3 = 1.5$, x/c = (♦) 5.66, (♦) 5.69, (♦) 5.71, (♦) 5.74, and (♦) 5.76.*

separation, along with two equidistant ($\Delta x/c = 0.025$) upstream and downstream profiles. The symbol size increases in the downstream direction. Figures 9a – c show the base ($C_\mu = 0$) flow for reference. The base flow evolution indicates the expected cross stream stretching of the velocity profiles as they approach separation due to the imposed adverse pressure gradient, even over a rather short streamwise distance. The vorticity flux (Figure 9b) indicates that peak levels are displaced away from the surface along with the velocity stretching through separation, while the peak magnitude decreases rather notably. This decrease in the vorticity flux levels through separation can be attributed to some of the vorticity being trapped within the separation bubble. While the peak levels of vorticity flux decrease and are displaced away from the surface through separation, the peak levels of TKE actually increase through separation, while again, being displaced away from the wall (Figure 9c). Clearly, increasing levels of TKE are expected as the boundary layer transitions into a shear layer past the separation point. The actuated flow velocity profiles through separation (Figure 9d) exhibit an increased cross-stream scale, extended linear central region, and formation much like a shear layer shape even at the flow separation point. Unlike the unactuated flow evolution (Figure 9a), there is a very slow progression in the mean velocity profiles through separation despite the sharp pressure gradient. Furthermore, the corresponding vorticity flux distributions (Figure 9e) are broadened but the peak levels are about halved when compared to the base flow at separation. Similarly, the TKE profiles (Figure 9f) exhibit about the same reduction in magnitude compared to the base flow, although the peak levels still weakly increase and migrate away from the wall as the flow evolves through separation.

The evolution of the flow through reattachment is also examined by extracting profiles through the reattachment region, similar to the assessment of the flow through separation, for the controlled ($C_\mu \cdot 10^3 = 1.5$) and uncontrolled flows. Figures 10a – c, again, present the five characteristic profiles of the wall-normal mean velocity, vorticity flux, and TKE for the base flow condition,

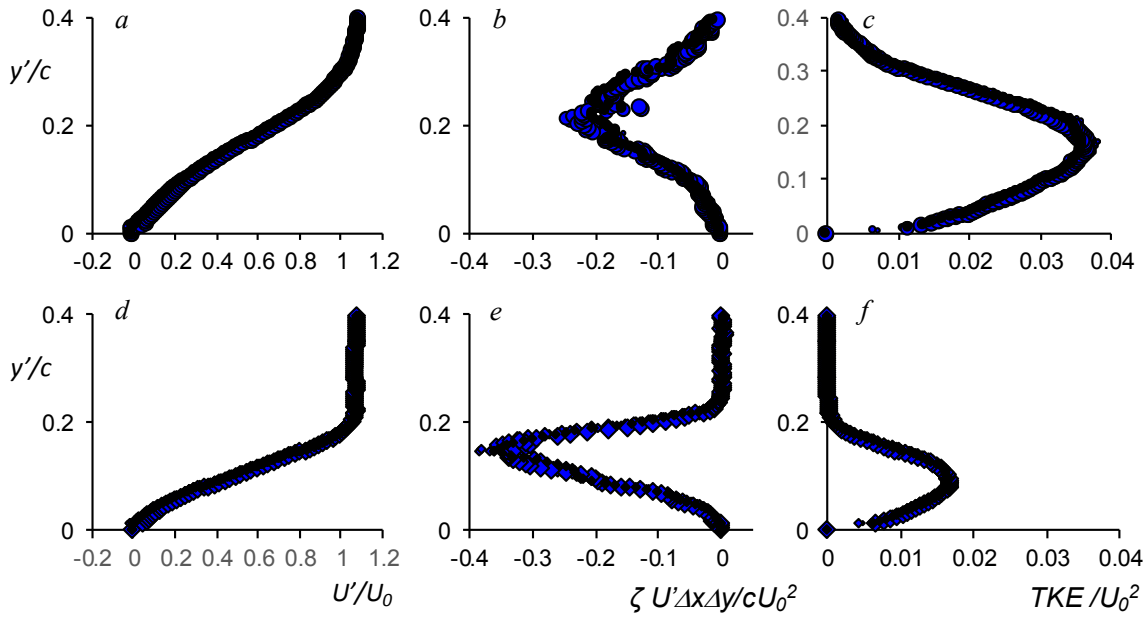

Figure 10. *Evolution of the mean velocity (a,d), vorticity flux (b,e) and turbulent kinetic energy (c,f) profiles through the flow reattachment for $C_\mu \cdot 10^3 = 0$ (a–c) and 1.5 (d–f). Symbol size increases in the downstream direction, and black symbols are associated with the separation point. At reattachment for $C_\mu \cdot 10^3 = 0$, x/c = (·) 6.43, (•) 6.45, (•) 6.48, (•) 6.50, and (•) 6.53, and for $C_\mu \cdot 10^3 = 1.5$, x/c = (♦) 5.90, (♦) 5.92, (♦) 5.95, (♦) 5.97 and (♦) 6.00.*

while the controlled-flow profiles are shown in Figures 10d – f. The first observation that is common to all of these profiles is that, although spaced exactly the same distance as through the separation region (Figure 9), all of these profiles show little progression from just upstream to just downstream of the reattachment point, where the profiles exactly at reattachment are shown in black symbols. As it was argued before in connection to Figure 3, the slowly-evolving flow at reattachment is attributed to the absence of the geometrically-imposed adverse pressure gradient that terminates upstream from the flow reattachment. Base flow reattaching velocity profiles (Figure 10a) impose shear across the full domain, having the inflection point displaced far away from the surface. Consequently, vorticity flux (Figure 10b) is also stretched across the whole measured domain, having a nearly symmetrical cross-stream distribution. It is interesting to note that the vorticity flux at the reattachment is much lower than at the separation in the base flow, suggesting a strong dissipation of vorticity through the separation bubble. Contrary to this observation, however, the turbulent kinetic energy distribution at reattachment (Figure 10c) indicates an increase in both the extent and magnitude relative to the separation point, as can be expected due to the shear layer and large scale structure development near reattachment. When comparing the mean controlled (Figure 10d) and uncontrolled (Figure 10a) velocity profiles, clearly the dominant shear at reattachment becomes much more compressed in the controlled flow conditions, which inherently confines both vorticity and its flux (Figure 10e) closer to the surface. Along with this compression, peak vorticity flux levels increase relative to the base reattaching flow (Figure 10b), but do not change much relative to the controlled flux magnitude at separation (Figure 9e). Contrary to amplification of the vorticity flux, the TKE at reattachment (Figure 10f) becomes not only confined closer to the surface, but more importantly it is significantly suppressed in magnitude when compared to the reattaching base flow (Figure 10c). This is attributed to the significant suppression of the separation bubble (cf. Figure 8), where the separating shear layer

reattaches shortly after its origin, without much distance to induce enhanced mixing and entrainment of the surrounding fluid that would also enhance the TKE.

Changes in the flow dynamics with separation delay is examined through distributions of the turbulent stresses at separation and reattachment for the base and three controlled cases that were discussed in Figure 6. Turbulent normal ($\overline{u'u'}$) and shear ($\overline{u'v'}$) stresses are shown in Figures 11a and b at the local separation, and in Figures 11d and e, at their local reattachment points. The base flow profiles are shown in open symbols, as a reference. First, the high levels of normal stresses are associated with a near-wall region in all of the cases (Figure 11a) in the separating flow. As the lowest C_μ increases the downstream end of the separation bubble, the peak normal stress levels also increase relative to the base flow. Its magnitude response then reverses as the bubble shortens with higher C_μ but, the peak normal stress becomes displaced further away from the surface. This is attributed to the separation point being displaced downstream with C_μ, into the geometry-induced adverse pressure gradient. Still, the overall magnitude is about half of that of the base flow. Presumably the most interesting flow control effect is seen in the changes on the turbulent shear stress profiles at separation (Figure 11b). Although the fixed coordinate system calculations of the turbulent stress (cf. Figure 7) imply a single sign ($\overline{u'v'}$), a different insight is gained by decomposing the instantaneous velocity fields into such wall-normal coordinates. Here, it is seen in Figure 11b that even in the base flow there is a change in sign in the shear stress, which is negative close to the wall and then switches sign, only to barely switch it again to negative before vanishing. The most significant consequence of the changing sign of $\overline{u'v'}$ in shear flows stems from the dominant production term in the turbulent kinetic energy $-\overline{u'v'}\cdot dU'/dy'$, which, with the dU'/dy' being positive, implies that this production term becomes negative everywhere $\overline{u'v'}$ is positive, meaning that instead of production of TKE, this terms drains TKE from the flow field. Hence, the base flow suggests that this term predominantly drains TKE in a layer away from the wall, while producing it in a layer closer to the wall. This distribution becomes altered for the

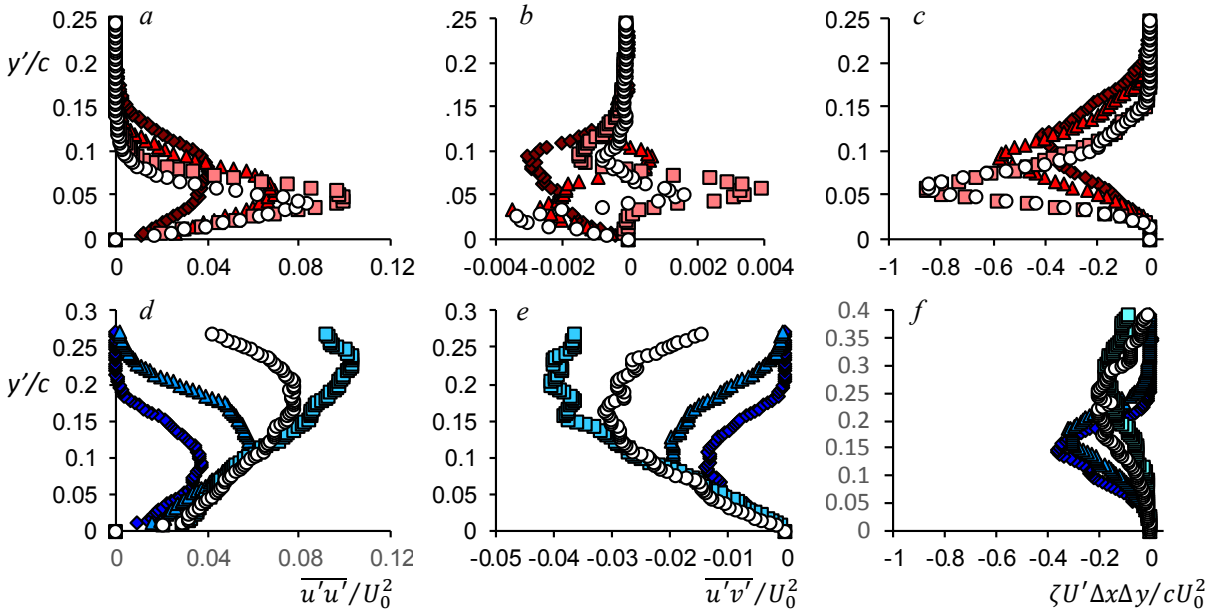

Figure 11. *Evolution of the turbulent normal (a,d) and shear (b,e) stresses, and the vorticity flux (c,f) at separation (a–c) and reattachment (d–f) for the base (○, M = 0.25) and the flow controlled by $C_\mu\cdot10^3$ = 0.36 (□), 0.96 (Δ), and 1.5 (◊). At* ***separation*** *x/c = (○) 5.32, (■) 5.27, (▲) 5.53, (♦) 5.71 and at* ***reattachment*** *= (○) 6.48, (■) 6.59, (▲) 6.20, (♦) 5.95.*

lowest C_μ, where almost no effect of this term is measured close to the wall, while the negative production is amplified further away. This trend completely changes for the two highest C_μ levels, where the drain of TKE becomes suppressed in this production term, particularly for the highest C_μ, where $\overline{u'v'}$ remains negative throughout the separation domain. Clearly, the full set of terms (in wall-normal coordinates) would need to be considered for a comprehensive TKE production analysis. At reattachment, the normal and shear stresses almost appear mirrored due to the consistent negative sign of $\overline{u'v'}$, but otherwise their evolution with C_μ is similar. At the lowest actuation level, both parameters increase in magnitude relative to the base flow, especially at the outward bound of the shear layer (cf. Figure 6a). However, once the flow control is effective in delaying flow separation, the magnitudes of both stresses decrease, while their peaks become increasingly shifted towards the surface and not associated with the outer edge of the shear layer, but rather about the highest shear zone. Overall, there is up to a twofold decrease in their magnitudes as measured relative to the base flow levels. Further insight into the changes in flow dynamics is gained by examination of profiles of the vorticity flux at the local separation and reattachment points, which are shown in Figures 11c and f, respectively. Vorticity flux distributions at local flow separation (Figure 11c) are, as expected, tied to the incoming near-wall shear of the stretched boundary layer. It is interesting that the lowest level of actuation practically has no effect on this incoming flux, although the separation point does slightly move downstream (cf. Figure 8a). Possibly even more prominent, is that the vorticity flux decreases with further delay of the separation, having peak levels displaced outward, despite the larger extent of the wall surface being traversed, which should facilitate further production of vorticity, however, it appears the flow control is offsetting this production, as vorticity dissipation and redistribution might be enhanced as well, as the flow travels further along the surface. All the vorticity flux levels at reattachment (Figure 11f) are significantly lower than those at separation, suggesting high rates of vorticity dissipation (and redistribution into other components) in the flow traversing over the separated domain. Contrary to the separation point, there is some noticeable outward displacement of the flux distribution for the lowest C_μ. with higher C_μ peak levels of vorticity flux becoming displaced closer to the wall, as the separation bubble end point retreats upstream, and furthermore, their peak levels increase in magnitude.

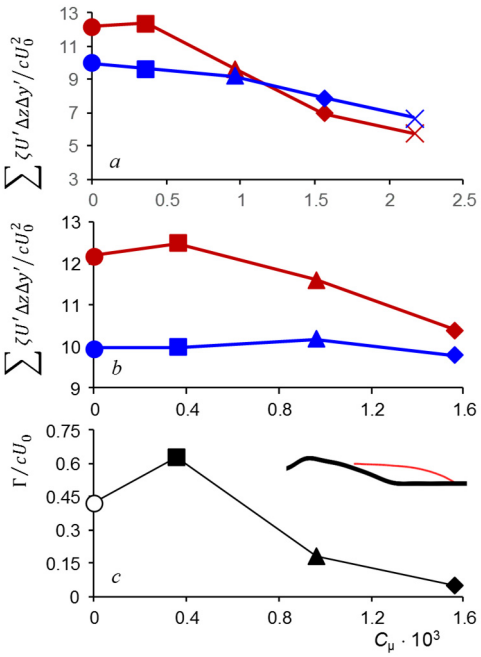

Figure 12. *Evolution of the total vorticity flux at separation (red) and reattachment (blue) of the base flow (a) and migrated separation/reattachment points (b), and the total circulation of the separated domain (c), with jet momentum coefficient C_μ. Separation domain bounds are illustrated in inset plot.*

Figure 12 summarizes the integral changes of the vorticity flux at local separation and reattachment with increasing flow control parameter C_μ. First, these fluxes are integrated across the fixed base flow separation and reattachment locations, regardless of the separation bubble domain location and size variation with C_μ, and are shown in Figure 12a. It is seen that for the base flow ($C_\mu = 0$) and up to $C_\mu \cdot 10^3 = 0.96$, there is a higher total vorticity flux at separation than at the

reattachment point. It should be noted that all of the vorticity flux at the separation point actually diverts around the bubble (in the average sense). The reduction in flux at the reattachment, however, implies that despite the fact there is no vorticity generation over the bubble's virtual outer boundary, the flow control presumably enhances the vorticity dissipation and redistribution. However, this trend reverses for the highest C_μ, up to full flow attachment, where more vorticity efflux is measured than that of the influx at the base flow separation. This is correlated with the increasing surface area for which vorticity production is occurring as the bubble shrinks with C_μ, as well as a possible reduction in vorticity dissipation over the less significant recirculating domain. A different perspective is gained when the influx and efflux are always anchored to the local separation and reattachment points, which is illustrated in Figure 12b. Namely, the influx at the bubble formation domain remains always higher than the efflux past the bubble. Given that no vorticity production exists about the bubble itself, the difference between the two fluxes incorporates all the vorticity dissipation and redistribution about the separated region. As the bubble keeps shrinking with C_μ, the separation and reattachment points keep approaching each other, which would imply that at the point of the bubble disappearance, efflux should match the influx. The measured trend in the difference between the two indicates an approach to the bubble disappearance closely past the highest C_μ shown. Prior analysis focuses on the vorticity evolution about the recirculating domain. To quantify the recirculating bubble dynamics, its circulation is extracted from the PIV fields, where the dividing streamline is defined for each of the four characteristic flow fields. The change in bubble circulation with the flow control parameter C_μ is shown in Figure 12c, while the base flow bubble boundary is shown in its inset. Not surprisingly, as the recirculating domain increases for the lowest C_μ, it traps more vorticity and its circulation increases. However, once the flow control suppresses the bubble, the bubble in turn releases vorticity and adjusts the circulation of the remaining trapped vorticity. Several-fold reduction in the controlled circulation, relative to the base flow, is estimated from the flow field measurements.

V. Scaling of the Time-Averaged Flow

A characteristic feature of flow approaching separation due to an adverse pressure gradient is that its shear stress at the wall approaches zero, and Elsberry et al. [15] postulated that this diminishes the importance of the wall region relative to the outer region on the flow approaching separation. Recently, Schatzman and Thomas [21] proposed a scaling of the adverse pressure gradient flow that, instead of traditional boundary layer wall scaling parameters, utilizes such outer shear layer parameters, expressed through the shear layer vorticity thickness and velocity deficit at the inflection point. They demonstrated excellent scaling of their experimental data and extended it to other available data in the literature. In principle, the proposed scaling was shown to be applicable to different flows undergoing separation due to adverse pressure gradients, with a deviation close to the wall, as can be expected from applying outer scaling parameters. This embedded-shear scaling was further applied to not only natural boundary layers in adverse pressure gradients, but also to natural and the flow-control delayed separation in a diffusing duct that resulted in an open separation domain [22]. Furthermore, extended dual-layer scaling was proposed for the mean velocity profiles exhibiting dual inflection points.

The present work postulates that the outer shear dominates not only the flow prior to separation in adverse pressure gradient, but also past the reattachment point, in the finite separated domain defined by the separation bubble. Therefore, both the mean velocity profiles at separation (Figure 6a) and reattachment (Figure 6b) for the base and three controlled cases are scaled by their local embedded shear layer vorticity thickness $\delta_\zeta = (U'_e - U')_{IP}/(dU'/dy)_{IP}$, and the ensuing

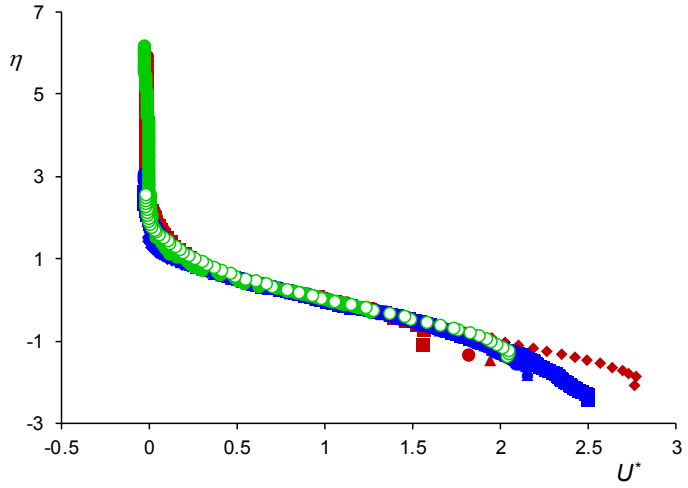

Figure 13. *Mean velocity profiles at separation (Figure 6a) and reattachment (Figure 6b) scaled by the embedded shear layer scaling [21]. Overlaid are the scaled mean velocity profiles for the natural and controlled flow separation in a diffusing duct [○, 22]. At separation x/c = (○) 5.32, (■) 5.27, (▲) 5.53, (♦) 5.71 and at reattachment = (○) 6.48, (■) 6.59, (▲) 6.20, (♦) 5.95.*

local velocity deficit $U'_d = (U'_e - U')_{IP}$, where the subscript *IP* designates the inflection point in the embedded shear layer. The resulting non-dimensional variables are $\eta = (y' - y'_{IP})/\delta_\zeta$ and $U^* = (U'_e - U')/U'_d$ for the length and velocity parameters respectively [21]. Where U'_d is the velocity deficit between the apparent free stream velocity (U'_e) and the velocity at the inflection point (U'). The resulting scaled profiles are shown in Figure 13. In addition to the current data, the equivalently-scaled mean velocity profiles of the uncontrolled and controlled open separation domain in the diffuser duct [22] are overlaid on the same plot. Remarkably, all of the scaled profiles reasonably collapse onto the unified profile, having an expected breakdown as they approach to the surface (high U^*). The robustness of this scaling, which in the present data includes natural and controlled flow separation in adverse pressure gradients within both open and closed separation domains, exemplifies that the dominant shear (i.e. embedded shear) away from the wall governs the ensuing flow. Since this shear is no longer contained in a narrow wall region, such as for a turbulent boundary layer over zero or near-zero pressure gradients, this dominant region for the flow evolution is not confined just to the wall region. Moreover, as the flow approaches separation, the shear in the near-wall region approaches zero, fully indicating the importance of the embedded shear away from the wall.

VI. Conclusions

The characteristics of a closed flow separation domain that forms in an adverse pressure gradient over a 2-D curved surface at $M = 0.25$ are investigated in wind tunnel experiments with emphasis on structural details of the flow as it undergoes separation and reattachment in the presence and absence of fluidic control. Actuation is effected by a spanwise array of fluidic oscillating jets whose momentum coefficient C_μ can be regulated over a broad range (typically below $2 \cdot 10^{-3}$). The migration of both the upstream and downstream edges of the separated flow domain and alteration of its global scale by the actuation are investigated using high-resolution planar particle image velocimetry (200 Hz) with spatial vector resolution of ~0.25 mm. The global flow field is obtained using composites of individual PIV images that include the ensemble-averaged separated flow domain. The PIV measurements are augmented by surface static pressure measurements.

While the separation is slightly delayed at low C_μ ($C_\mu \cdot 10^3 = 0.36$), the reattachment is displaced even farther downstream, resulting in a net increase in the characteristic length of the separated domain (about 15%). As C_μ is increased, gradual reversal and receding of reattachment is coupled with strong streamwise progression of the separation location which leads to a sharp overall decrease in the length of the recirculating domain. Finally, as the separation domain is nearing

complete extinction, its response to increases in C_μ is slow and nearly-asymptotic. Along with the varying responses of the leading and trailing edges of the separation domain to the actuation, differences in the time-averaged velocity and turbulent stresses at separation and reattachment are assessed. It is shown that, as a result of the changes in the streamwise pressure gradient between the upstream and downstream ends of the separation domain, the streamwise evolution of the respective cross-stream velocity distributions varies from rapid streamwise evolution through separation to slow nearly imperceptive changes through attachment. Furthermore, while the actuation nearly halves the turbulent kinetic energy of the base flow at both separation and reattachment, the magnitude of the cross-stream vorticity flux decreases at separation but remains nearly invariant at reattachment.

Perhaps the most salient finding of the present investigation is the extension of an earlier observation [19] that, close to separation, the vanishing (time-averaged) shear stress at the surface implies that the importance of the wall region relative to the flow dynamics at separation diminishes in comparison with the effects of the outer shear layer flow. The significance of the outer 'embedded' shear layer was formulated following the scaling of the velocity distribution proposed by Schatzman and Thomas [21]. The present findings imply that the outer shear dominates not only the separating flow but also the reattaching flow. Following the demonstration of the scaling in "open-ended" separation in a diffuser duct [22] in the absence and presence of flow control, the present work considers the scaling of cross-stream velocity distributions at the upstream (separating) and downstream (reattaching) ends of a controlled closed separation domain. It is shown that, despite the clear differences between the cross-stream scales of the time-averaged velocity distributions at separation and reattachment in the presence and absence of actuation, scaling of these distributions by their local vorticity layer thickness and velocity deficit yields remarkable "universal" collapse, except very close to the surface. Moreover, the scaled velocity distributions of the open separation [22] in the presence and absence of actuation also collapse on top of the scaled distribution of the closed separation.

The similarity of the time-averaged, scaled, shear velocity profiles implies that these flows are driven by a similar (inviscid) mechanism regardless of their different geometries or the fact that they separate naturally or following prolonged attachment by flow actuation. While the similarity implies that these separating flows in adverse pressure gradients may be governed by a similar inviscid mechanism (as already noted for open flow separation [22]), at present, there is no evidence that the Reynolds stresses can also be scaled in the same manner and accordingly it cannot be argued that details of the flow dynamics are equivalent.

References

[1] Ethier, C. R., Prakash, S, Steinman, D.A., Leask, R.L., Couch, G.G. and Ojha, M., "Steady flow separation patterns in a 45 degree junction," *J. Fluid Mechanics*, **411**, pp. 1-38, 2000.

[2] Blanckaert, K., "Flow separation at convex banks in open channels," *J. Fluid Mechanics*, **778**, pp. 432-467, 2015.

[3] Papadopoulos, G., and. Otugen, M. V., "Separating and reattaching flow structure in a suddenly expanding rectangular duct," *J. Fluids Eng*., 117, pp. 17-23,1995.

[4] Yang, William, and Benny Kuan. "Experimental investigation of dilute turbulent particulate flow inside a curved 90 bend." *Chemical Engineering Science*, 2006; Vol 61 no. 11, pp. 3593-3601.

[5] Suzuki, T., Colonius, T. and Pirozzoli, S., "Vortex shedding in a two-dimensional diffuser: theory and simulation of separation control by periodic mass injection," *J. Fluid Mechanics*, **520**, pp. 187-213, 2004.

[6] Amitay, Michael, Dale Pitt, and Ari Glezer. "Separation control in duct flows." Journal of Aircraft, 2002; Vol 39 no. 4; pp. 616-620.

[7] Kumar,V., Alvi,F.S., "Use of high-speed microjets for active separation control in diffusers," AIAA J., 44, pp. 273-281, 2006.

[8] Banaszuk, A., Narayanan, S. and Zhang, Y., "Adaptive control of flow separation in a planar diffuser," *AIAA Paper* 2003-617, 2003.

[9] Vaccaro, J.C., Elimelech, Y., Chen, Y., Sahni, O., Jansen, K.E. and Amitay, M., "Experimental and numerical investigation on steady blowing flow control within a compact inlet duct," *Intl J. Heat Fluid Fl.*, **54**, pp. 143-152, 2015.

[10] Simpson, R.L., "Turbulent boundary-layer separation," *Annu. Rev. Fluid Mech.*, **21**, pp. 205-231, 1989.

[11] Chun, Kyung-Bin, and Sung, H. J., "Control of turbulent separated flow over a backward-facing step by local forcing," Exp. Fluids, 21, pp. 417-426, 1996.

[12] Yoshioka, S., Obi, S., and Masuda, S., "Organized vortex motion in periodically perturbed turbulent separated flow over a backward-facing step," Intl J. Heat Fluid Fl., 22, pp. 301-307, 2001.

[13] Vukasinovic, B., Rusak, Z., and Glezer, A., "Dissipative Small-scale Actuation of a Turbulent Shear Layer," *J. Fluid Mechanics*, **656**, pp. 51-81, 2010.

[14] Pauley, L., Moin, P., and Reynolds, W., "The structure of two-dimensional separation," *J. Fluid Mech*, **220**, pp. 397-411, 1990.

[15] Kiya, M., Sasaki, K., "Structure of a turbulent separation bubble," *J. Fluid Mech.*, **137**, pp 83-113, 1983.

[16] Kiya, M., Sasaki, K., "Structure of large-scale vortices and unsteady reverse flow in the reattaching zone of a turbulent separation bubble," *J. Fluid Mech.*, **154**, pp 463-491, 1985.

[17] Dandois, J., Garnier, E., and Sagaut, P., "Numerical simulation of active separation control by a synthetic jet," *J. Fluid Mech.*, **574**, pp 25-58, 2007.

[18] Marusic, I. and Perry, A.E., "A wake model for the turbulent structure of boundary layers. Part 2. Further experimental support," *J. Fluid Mechanics*. **298**, pp. 389 – 407, 1995.

[19] Elsberry, K., Loeffler, J., Zhou, M.D., and Wygnanski, I., "An experimental study of a boundary layer that is maintained on the verge of separation," *J. Fluid Mechanics*. **423**, pp 227-261, 2000.

[20] Castillo, L. and George, W.K., "Similarity analysis for turbulent boundary layer with pressure gradient: outer flow," *AIAA Journal*. **39(1)**, pp 41-47, 2001.

[21] Schatzman, D.M., and Thomas, F.O., "An experimental investigation of an unsteady adverse pressure gradient turbulent boundary layer: embedded shear layer scaling," *J. Fluids Mechanics*, **815**, pp. 592-642, 2017.

[22] Peterson, C.J., Vukasinovic, B., and Glezer. A., "Characterization of controlled flow separation," *AIAA Paper 2018-1282*, 2018.